# Microphysical properties of various precipitation systems worldwide classified via objective methods based on dual-frequency precipitation radar observations

Yujia Zhang[1,2] Xiaodong Zhang[1,2], Xiang Ni[1,2]

[1]Chongqing Jinfo Mou ntain Karst Ecosystem National Observation and Research Station, School of Geographical Sciences, Southwest University, Chongqing, China
[2]Chongqing Engineering Research Center for Remote Sensing Big Data Application, School of Geographical Sciences, Southwest University, Chongqing, China

*Correspondence to*: Xiang Ni (nixiang@swu.edu.cn)

**Abstract.** Microphysical properties play crucial roles in physical processes related to the development of precipitation. In this study, Global Precipitation Measurement (GPM) dual-frequency precipitation radar (DPR) data were processed to demonstrate the microphysical properties of different precipitation systems (PSs) that are objectively classified with the k-means clustering algorithm. Four types of regular/non-extreme PS (high-latitude shallow PS, subtropical shallow PS, moderate PS, deep PS) and four types of extreme PS (extreme deep PS, strong PS, extreme strong PS, and marine extreme PS) were recognized. These eight types of PS exhibit differences in spatial-temporal features and convection characteristics, such as storm height, rain intensity, and vertical structures. For example, the extreme strong PS, with the highest radar echo top and largest mean mass-weighted mean diameter, mainly locate over tropical continent, whereas high-latitude shallow PS have the least precipitation rate and mean normalized intercept parameter values. The relationships between convection features and microphysical properties also vary among the eight types of PSs. For extreme PS, maximum precipitation rate near the surface generally exceeds 100 mm $h^{-1}$ and balanced breakup and coalescence processes play a dominant role compared with non-extreme PS. In contrary, the coalescence processes dominate near the surface in two types of shallow PS. These results highlight the diversity of global precipitation microphysics and emphasize the necessity of global studies to increase the understanding of precipitation processes.

## 1. Introduction

The microphysical characteristics of precipitation provide crucial information for describing precipitation. The deficiency of precipitation microphysical parameterization schemes is a significant factor contributing to precipitation errors in weather and climate models (Snook and Xue, 2008). Accurately obtaining spatiotemporal variations in precipitation microphysical parameters is essential for understanding the physical processes of precipitation, increasing the accuracy of quantitative precipitation estimation, and evaluating microphysical parameterizations in models (Chen et al., 2011; Zhang et al., 2023). Currently, observations and characteristics of precipitation microphysics at the global scale remain lacking because of the limited number of observation approaches.

The drop size distribution (DSD) is a typical metric for depicting precipitation microphysics. DSD features can be derived from observations obtained via disdrometers, ground-based radar instruments, and space-based radar instruments. In radar instruments, the interaction of electromagnetic waves with hydrometeors is used to retrieve DSD parameters (Marzuki et al., 2023), whereas disdrometers measure raindrop counts to directly obtain DSDs at the surface. Disdrometers provide only point measurements at specific levels and cannot measure the vertical structure of DSDs. Moreover, disdrometers have not been deployed globally, especially over the ocean. Although ground-based radar instruments can measure the three-dimensional structure of precipitation, they can only be used in limited areas, and their observation accuracy is significantly affected by the terrain conditions within the observation area (Dai et al., 2020). In contrast, space-based radar instruments can provide the vertical structures of DSD parameters worldwide. This study focused on the microphysical characteristics of various precipitation systems (PSs) worldwide. Compared with other instruments, space-based radar instruments are the most suitable for researching global precipitation microphysics.

In 1997, the Tropical Rainfall Measuring Mission (TRMM) satellite was launched by the National Aeronautics and Space Administration (NASA) and the Japan Aerospace Exploration Agency (JAXA). The precipitation radar (PR), which operates in the Ku-band (13.8 GHz), was carried by the TRMM (Iguchi et al., 2000). This marked the beginning of the observation of precipitation microphysics via space-based radar instruments. Notably, DSD parameters were retrieved from the radar reflectivity measured by the PR with the assumption that the DSD can be characterized by the diameter parameter itself (Iguchi et al., 2000). As a result, the DSDs obtained via retrieval exhibited large errors. In 2014, NASA and JAXA successfully launched the Global Precipitation Measurement (GPM) Core Observatory (GPM-CO). The GPM-CO carried the first spaceborne dual-frequency precipitation radar (DPR) system, operating in the Ku and Ka bands (13.6 and 35.5 GHz, respectively) (Skofronick-Jackson et al., 2017). Via the use of this characteristic, mean mass-weighted mean diameter ($D_m$) and mean normalized intercept parameter ($N_w$) can be retrieved. The retrieved DSD parameters have been verified with ground-based observations and are better than those obtained via the TRMM PR algorithm (Sun et al., 2020). In addition, validation studies have confirmed the feasibility of using DPR observations for DSD parameter analysis (D'Adderio et al., 2018; Peinó

et al., 2024). Peinó et al. (2024) used observational data from seven Parsivel disdrometers across different topographic zones in the western Mediterranean to validate GPM DSD products. They reported that the GPM DPR products effectively captured the variations in DSDs observed under different rainfall intensities. Therefore, GPM DSD products have been widely employed to investigate the microphysical characteristics of precipitation in the literature (Wen et al., 2024, 2023) .

However, previous studies involving GPM DSD products have focused mainly on specific locations or weather systems. For example, Li et al. (2024) studied the vertical structure and DSD characteristics of different precipitation types during the rainy season over South China and reported that the precipitation type and intensity affect the DSD parameters. In their study, under the same precipitation intensity, shallow convective precipitation exhibited the smallest $D_m$ and largest $N_w$ values, whereas deep convective precipitation exhibited the opposite phenomenon. Additionally, regarding stratiform precipitation, for Precipitation Rate > 3.5 mm $h^{-1}$, $D_m$ slightly increased, and in regard to shallow convective precipitation, $D_m$ remained at approximately 1.3 mm for Precipitation Rate > 2 mm $h^{-1}$. Similarly, Wen et al. (2023) analyzed the seasonal variations in the vertical structure of precipitation microphysics in East China. They reported that the spatial distributions of $D_m$ and $N_w$ demonstrate obvious seasonal variations and that there are more small raindrops in convective precipitation in autumn and winter than during the other seasons. These studies revealed the variations in microphysical characteristics across different seasons and rainfall types. Additionally, regarding weather conditions, regional variations in the precipitation characteristics of tropical cyclones have been investigated over the North Indian Ocean (Kumar et al., 2023). Research has revealed that the nature of microphysical processes largely influences the growth of droplets in convective and stratiform rain. Wu et al. (2022) investigated the DSD characteristics of record-breaking Typhoon In-Fa. Their findings revealed significant internal and regional differences in the microphysical characteristics of typhoon precipitation. When different precipitation types during Typhoon In-Fa were compared, convective precipitation ($N_w$ values ranging from 3.80 to 3.96 $m^{-3}$ $mm^{-1}$) exhibited higher raindrop concentrations than did stratiform precipitation ($N_w$ values ranging from 3.40 to 3.50 $m^{-3}$ $mm^{-1}$). Additionally, convective precipitation during Typhoon In-Fa indicated a greater (lower) raindrop concentration than that during Typhoon Taiwan (Hainan), while the raindrop diameter was smaller than those during both Typhoons Taiwan and Hainan. These studies primarily focused on the microphysical process and structure of various weather conditions, which provided insight into the formation process of precipitation. At present, there are few studies on the microphysical characteristics of large-scale and global PSs. On the one hand, as mentioned above, the DSD is influenced by numerous factors, such as precipitation type and season. There may be multiple precipitation types and DSDs in one area. On the other hand, few DSD datasets covering the whole world are available. Dolan et al. (2018) used twelve disdrometer datasets across three latitudinal zones—high-latitude, midlatitude, and low-latitude zones—to analyze DSD spatial variability. They reported that the DSD varies with latitude. At low latitudes, moderate $D_m$ values (1.5–2 mm) and large log10($N_w$) values (> 4 $m^{-3}$ $mm^{-1}$) dominated. At midlatitudes, high $D_m$ values and small $N_w$ values dominated. At high latitudes, low $D_m$ and large $N_w$ values prevailed. Although the dataset covered a wide range of precipitation regimes, it could not capture all rain regimes. Moreover, a regional DSD dataset cannot

represent the DSD within a given latitudinal band because of the limitations of disdrometers. Hence, in this study, GPM DSD products were employed to investigate the microphysical characteristics of PSs at global scales.

This study aimed to classify different PSs on the basis of DPR observations via machine learning and to analyze the microphysical characteristics of different types of PSs. The results could address regional DSD variability and increase our understanding of the microphysical processes of different types of PSs. This study is organized in four sections. Section 2 provides detailed descriptions of the GPM data and machine learning models applied in this study. The main results are presented in Section 3, and finally, a summary is given in Section 4.

## 2. Data and methods

### 2.1. Data

GPM observations cover the range from 65° S to 65° N (Hou et al., 2014; Tapiador et al., 2012). The GPM DPR operates in the Ka and Ku bands, with a spatial resolution of approximately $5 \times 5$ km$^2$. The scanning of DPR is cross-track and has three scan patterns: normal scan, matching scan, and high sensitivity scan (Das et al., 2022). Since the scanning pattern of the Ka-band was changed in 2018 (Awaka et al., 2021), the GPM 2A DPR (version 7) products considered the changes in the Ka-band scan pattern with a more accurate precipitation estimation algorithm. The product formats in version 7 have been changed from the original three types to two types: Full scan and High Sensitivity scan. The Full scan product exhibits a new format and is defined as a full-scan dual-frequency product with a 125-m vertical range resolution. Compared with previous algorithms, the Full Scan mode makes it possible for the first time to process a full-scan band of approximately 245 km in dual-band mode (Awaka et al., 2021). Therefore, the observations from the Full scan were adopted in this study.

In this study, five years (2018–2022) of 2A DPR products (version 7) were employed. The parameters used in this machine learning model include DSD parameters ($D_m$ and $N_w$), near-surface precipitation rate (mm h$^{-1}$), attenuation-corrected radar reflectivity (dBZ), reflectivity near the surface ($Z_{surf}$), and typeprecip (stratiform or convective), and airTemperature. Detailed descriptions of the generation and retrieval of these parameters can be found in Iguchi et al. (2021). The precipitation type helps distinguish between stratiform and convective precipitation pixels, while air temperature is used to separate snow from rain.

### 2.2. Precipitation system (PS)

This paper presents a method based on the connected domain principle for identifying PSs, similar to those contained in the widely used TRMM/GPM Precipitation Feature dataset (Liu et al., 2008, 2020). First, pixels with precipitation no less than

0.1 mm $h^{-1}$ are derived from DPR orbit data. Then, neighboring precipitation pixels, including diagonally adjacent precipitation pixels, are grouped together as a PS. Each PS is required to have a minimum of four precipitation pixels.

The DPR provides three-dimensional structure of precipitation and DPR products include radar reflectivity parameters and retrieved DSD parameters from 0 to 22 km with a range resolution of 125 m. Consequently, for each PS type, DSD and radar reflectivity parameters such as the maximum and average values of each layer were calculated. The average $D_m$ and $N_w$ profiles were used for each PS, and if the profiles of the maximum $D_m$ and $N_w$ values in each layer were involved, MAX-$D_m$ and MAX-$N_w$, respectively, were used. Given the potential relationships of the convective intensity with microphysical parameters, $Z_e$ in the product was employed to calculate several convection indicators. These include the maximum 20/30/40 dBZ echo top height (MAXHT20/30/40) for each type of PS (Liu, 2011; Liu et al., 2020; Ni et al., 2019; Roy et al., 2020), the echo top height of the PS ($H_{top}$) (Arulraj and Barros, 2021), and other convective parameters. To describe PS conditions, several additional features were calculated, including the maximum precipitation rate near the surface (maximum precipitation rate of the precipitation pixels included in the PS) and precipitation area (the number of precipitation pixels contained in the PS). For the stratiform, convective, land, and oceanic percentages, the corresponding pixel fractions among each individual PS were first calculated. These fractions were then averaged across all PSs within a given cluster to represent the cluster-level characteristics. Considering that the GPM satellite exhibits a higher observation frequency in high-latitude regions (approximately 2–3 times that at the equator), the original dataset is prone to oversampling in these areas, which can introduce bias. To construct a balanced dataset suitable for clustering analysis, this study implemented a homogenization for the sampling. Specifically, the satellite's observation frequency was calculated as a function of latitude, and sample size for each latitude was adjusted using the ratio of its frequency to that at the equator. Subsequently, precipitation systems were randomly selected from each latitude to ensure a consistent scaled sample size, thereby effectively addressing the issue of uneven sampling. Finally, a total of 8,924,307 PSs were obtained for subsequent analysis.

### 2.3. Methods

In this study, two distinct machine learning models, namely k-means clustering and principal component analysis (PCA) were used. Both models were trained and evaluated via the Python scikit-learn package. These models are briefly described below. The k-means algorithm is a widely used unsupervised clustering method in machine learning because of its simplicity and computational efficiency (Jain, 2010). The algorithm follows a three-step process. Initially, it aims to select initial cluster centers by randomly obtaining sample coordinates from the dataset and assigning each sample to its nearest cluster center. Next, it computes the mean of all sample points assigned to each previous cluster center to establish new cluster centers. Finally, the algorithm aims to evaluate the differences between the new and old cluster centers. If differences are present, the last two steps are repeated until the cluster centers stabilize and no longer shift (Jain, 2010).

PCA is a classical dimensionality reduction tool in machine learning (Gang and Bajwa, 2022). PCA is based on the linear combination of target features to construct the principal subspace, and the variance is then employed to measure the information content with the aim of identifying the linear subspace with the maximum variance (Marukatat, 2023). In summary, PCA aims to transform numerous pertinent features into a comparatively limited number of irrelevant ones, thereby retaining as much of the informational content of the original data as possible (Gang and Bajwa, 2022). Considering that there are 176 vertical layers of GPM DPR products, if all DSD data were used as input parameters, the clustering effect could be poor because of the high dimensionality. In this study, PCA was adopted to reduce the dimensionality of the data while striking a balance between information loss and the optimal number of parameters to be retained (Festa et al., 2023; Jolliffe and Cadima, 2016). Specifically, PCA was independently applied to the vertical profiles of $Z_e$, $D_m$, and $N_w$, each of which originally consists of 176 vertical levels. Finally, for each profile of $Z_e$, $D_m$, or $N_w$, the 176 vertical levels are reduced to one single value, which referred to as the first principal component score, capturing the dominant variation in the vertical structure.

In this study, all the ~9 million PSs derived in section 2.2 are used. Input parameters of each PS for k-means clustering include the maximum precipitation rate near the surface, $H_{top}$, the precipitation area, the proportion of stratiform precipitation, the proportion of convective precipitation, the DSD parameters ($D_m$ and $N_w$), the maximum $Z_e$, and the first principal component score of the vertical profiles of $Z_e$, $D_m$, and $N_w$. These parameters were selected based on their critical role in comprehensively characterizing the features, structure, and microphysical processes of precipitation systems. Among them, the maximum surface precipitation rate and $Z_e$ reflect the intensity of the precipitation process and its echo characteristics, while the precipitation area directly characterizes the spatial differences in both the vertical and horizontal distributions of the system. The $H_{top}$ not only reveals the vertical distribution but also captures the top-level information of the precipitation cloud through the maximum reflectivity height. Introducing the proportions of stratiform and convective precipitation facilitates the differentiation of precipitation types generated by distinct mechanisms, thereby elucidating their evolution patterns and dynamic characteristics. Furthermore, the DSD parameters ($D_m$ and $N_w$) effectively describe the size distribution of precipitation particles and their intrinsic physical processes, providing an essential basis for an in-depth understanding of precipitation microphysics. Collectively, constructing a multidimensional precipitation feature space with these parameters enhances the accuracy and robustness of the clustering analysis.

The quality of clustering was evaluated by analyzing different clustering structures derived from the same dataset. Common clustering performance metrics include the sum of squared errors (SSE), Davis Bouldin (DB) index, Calinski-Harabasz (CH) Score (El Khattabi et al., 2024) and silhouette index, which are widely used to evaluate clustering effectiveness and quality (Ay et al., 2023). In this case, the DB index was calculated by computing the average sum of the intraclass distances between any two clusters divided by the distance between the centers of those two clusters and obtaining the maximum value. The DB index can manage clusters of different sizes and densities with a high degree of robustness to noise and outliers. A lower DB index indicates better clustering performance (Sowan et al., 2023). Additionally, the CH score, which assesses clustering

compactness and separation, was also considered. Higher CH scores indicates better-defined clusters. Algorithms with clustering numbers ranging from 3 to 20 were executed, and the resulting change in the DB index and CH score was plotted (refer to Fig. S1 in the Supplementary Material). As shown in Figure S1, the DB index reaches its minimum at K = 8 and then increases rapidly, whereas the CH score attains its maximum at K = 11 with only a slight improvement compared to K = 8. Considering the overall trends of both indices, K = 8 provides a more balanced and stable clustering structure and was therefore selected as the optimal number of clusters.

## 3. Results and discussion

### 3.1. Global distributions

After clustering, each cluster was characterized by its unique precipitation and spatial distribution characteristics, including $D_m$, MAXHT20/30/40, and convective/stratiform fractions and so on. Table 1 summarizes the statistics of various parameters for the eight types of PS, while Figure 1 illustrates their spatial distributions. For clarity in the subsequent discussion, Clusters 1–8 were grouped and named based on their spatial distributions (Fig. 1) and key precipitation characteristics (Table 1). Four non-extreme precipitation systems were identified (high-latitude shallow, subtropical shallow, moderate, and deep PS), along with four extreme precipitation systems (extreme deep, strong, extreme strong, and marine extreme PS). Overall, extreme precipitation systems account for a smaller proportion and exhibit higher MAXHT20/30/40, larger $D_m$, and stronger precipitation rates compared with non-extreme precipitation systems. Geographically, high-latitude shallow precipitation systems are mainly distributed north of 40°N and south of 35°S, subtropical shallow precipitation systems occur primarily within about 20° on both sides of the equator, and marine extreme convection is mostly located over the ocean.

The numbers in Table 1 include abundant information and verify the rationality of the objectively clustering algorithm. First, the numbers of the various types of PSs differed significantly. The two types of shallow PSs (high-latitude shallow PS and subtropical shallow PS) accounted for 81.44% of the total PS count. The proportions of deep and moderate PSs were 2.41% and 15.50%, respectively. The other four types of PS are regarded as extreme PS (extreme deep PS, strong PS, extreme strong PS, and marine extreme PS) because their ratios of the total PS are less than 1%, accounted for only 0.39%, 0.22%, 0.02%, and 0.01%, respectively. In the non-extreme PS, MAXHT20 is generally positively related to the precipitation rate (Table 1). However, in the extreme PS, the correlation between the extreme precipitation rate and MAXHT20 is not clear. For example, that the mean value of the maximum precipitation rate in marine extreme PS was the highest among the eight types of PSs, although its MAXHT20 was less than that in extreme strong PS and close to that in extreme deep PS. This result is consistent with other studies noting a weak link between the heaviest rainfall and the highest storm top (Hamada et al., 2015). Although the convective intensity of extreme deep PS is not significantly higher than that of deep PS, it exhibits a substantially larger precipitation area and maximum precipitation rate.

High-latitude shallow PS was most prevalent at midlatitudes and high latitudes, where snowfall and sleeting are more frequent than at low latitudes. Notably, high-latitude shallow PS were dominated by stratiform precipitation, with stratiform pixels accounting for 88.63%. Meanwhile, approximately 86.60% of the PS exhibited surface temperatures higher than 0 °C. A study confirmed that at high latitudes and in polar regions, more than 25% of precipitation falls as snow (Lerber et al., 2018). This is consistent with the observations from high-latitude shallow PS. Additionally, an analysis of high-latitude shallow PS by latitude revealed that with increasing latitude, the number of samples generally increased. Moreover, the number of PSs with echo top heights less than 2.5 km increased with latitude. During the winter season at 65°S, PSs with echo top heights below 2.5 km accounted for approximately 50% of the total PSs there. This is likely due to the influence of the low surface temperature and weak convection (refer to Fig. S2 in the Supplementary Material).

Subtropical shallow PS primarily occurred over the ocean dominated by the subtropical high, with a relatively limited degree of overlap with moderate PS and deep PS (Fig. 1). The mean MAXHT20 value in subtropical shallow PS was only 3.29 km, and the proportion of convective precipitation was the highest among all the types of PSs, exceeding 90%. Compared with those of the other PSs, subtropical shallow PS exhibited the smallest precipitation area. Moreover, it was rarely found over land. These results support the conclusion that subtropical shallow PS is associated with isolated shallow convection over the ocean, which has been the topic of interest in previous studies (Chen and Liu, 2016; Chudler et al., 2022; Houze Jr. et al., 2015).

The geographic distribution patterns of deep PS and moderate PS were approximately the same (Fig. 1). The number of occurrences in the maritime continent (MC), Indian Ocean, Atlantic Ocean, Amazon rainforests and Pacific Ocean were relatively high. There regions are generally influenced by the Intertropical Convergence Zone (ITCZ). Nevertheless, the deep PS has higher land percentage. The mean values of the maximum precipitation rates in moderate PS and deep PS were 6.21, 35.94 mm $h^{-1}$, respectively, whereas those of MAXHT20 were 7.03 and 11.89 km, respectively. As a result, the spatial distribution of deep PS is very similar to that of the deep convection core (Ni et al., 2019), which is defined as MAXHT20 larger than 10 km.

Strong PS, extreme deep PS, extreme strong PS, and marine extreme PS demonstrated low sample sizes. However, their precipitation areas are significantly larger than non-extreme PS (Table 1). The location of extreme deep PS is similar with moderate and deep PS, with larger values for most parameters. In the extreme strong PS, the proportion of land pixels reaches 81%, with significant concentrations in near-equatorial Africa, America, India, the southeastern U.S., and South America. The average maximum precipitation rate in extreme strong PS was 156.37 mm $h^{-1}$, and MAXHT40 reached 12.32 km, which is the highest among all the types of PSs. The high MAXHT40 value indicates strong updraft in the middle troposphere, which is a hallmark of intense convection and favors hail formation (Kumar et al., 2023; Zipser et al., 2006). Therefore, the spatial distributions of hailstorms in extreme strong PS were very similar to those of the global hail map derived from spaceborne

253 precipitation radar (Ni et al., 2017) and passive microwave sensor (Bang and Cecil, 2021). Marine extreme PS was primarily
254 situated in the near-equatorial marine region, with only 943 PSs and 90% is over the ocean. The mean maximum precipitation
255 rate in marine extreme PS was 178.30 mm $h^{-1}$, ranking first among the eight types of PSs. Although the MAXHT20 value in
256 marine extreme PS reached 12.81 km, the MAXHT40 value in marine extreme PS was approximately half of that in extreme
257 strong PS, indicating low convection activity in the middle and upper levels. This is consistent with the findings of Liu et al.
258 (2007), who observed that the difference between cloud-top height and MAXHT20 over land is smaller than that over the
259 ocean, indicating that convective intensity is stronger over land than over the ocean.
260
261 Oceanic extreme PS (extreme deep PS and marine extreme PS) with a high fraction of ocean pixels, have mean precipitation
262 coverage area exceeding 36000 $km^2$, significantly larger than continental extreme PS (strong PS and extreme strong PS). This
263 spatial distribution aligns with previous findings that the most extensive precipitation systems are predominantly located in
264 oceanic regions according to the study of Zhang and Wang (2021) . Furthermore, continental extreme PS display markedly
265 stronger convective intensity. This disparity is largely attributable to the observation that the heaviest PS generally occur over
266 tropical land, the Western Pacific warm pool, the North American Great Plains, and Argentina, whereas the most severe
267 convective storms are predominantly observed over continental areas (Liu and Zipser, 2015).
268

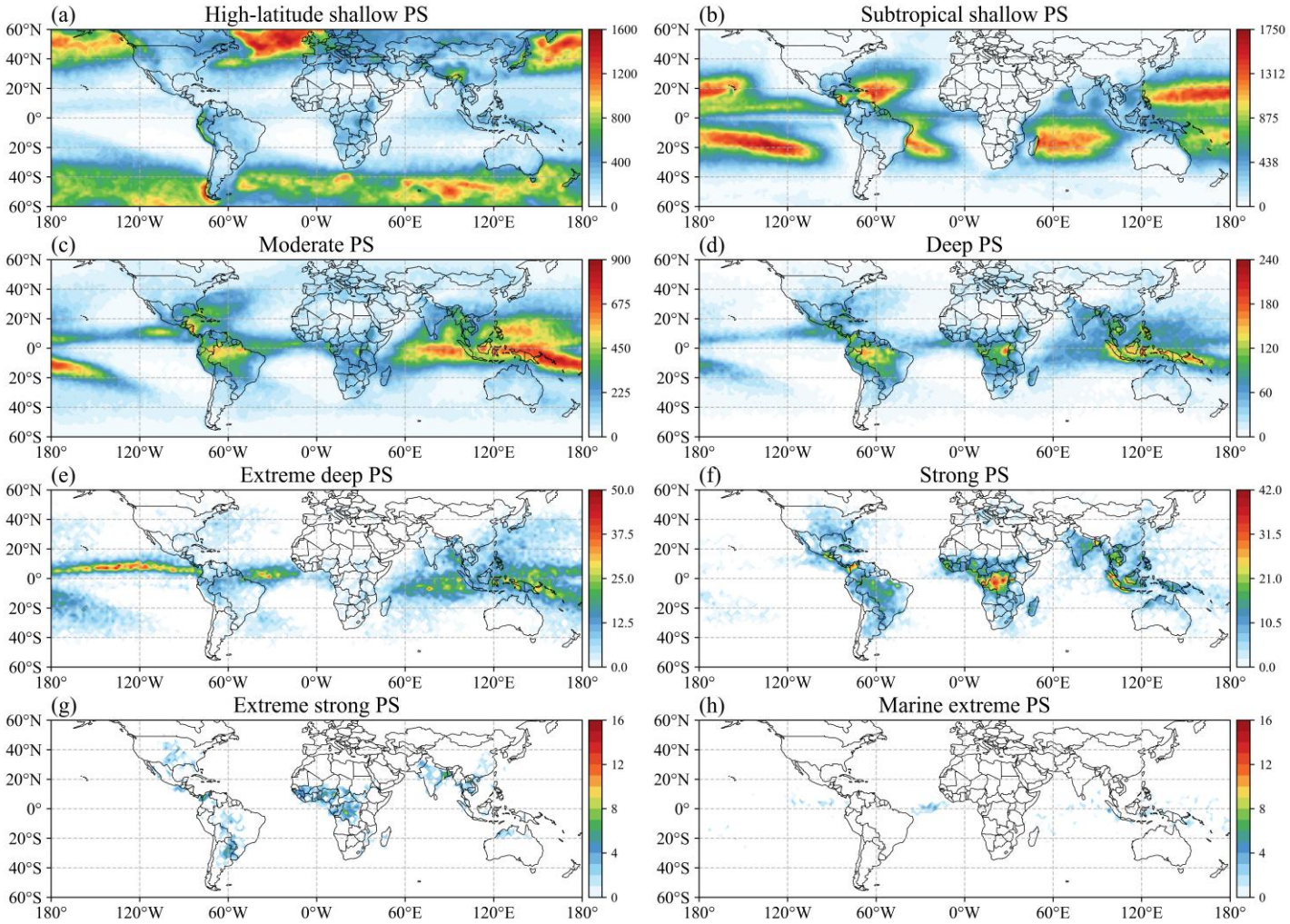


**Figure 1.** Spatial distributions (2° × 2°) of the PS counts from 2018 to 2022

**Table 1.** Precipitation parameters for the different types of PSs. (* indicate that in high-latitude shallow PS and subtropical shallow PS, approximately 80% of the samples do not reach 40 dBZ. Therefore, the mean MAXHT40 for these samples is recorded as 0.)

| | high-latitude shallow PS | subtropical shallow PS | Moderate PS | deep PS | extreme deep PS | strong PS | extreme strong PS | marine extreme PS |
|---|---|---|---|---|---|---|---|---|
| Mean MAXHT20 (km) | 3.40 | 3.29 | 7.03 | 11.89 | 12.67 | 15.39 | 17.21 | 12.85 |
| Mean MAXHT30 (km) | 2.63 | 2.67 | 5.11 | 8.65 | 8.52 | 13.68 | 16.31 | 9.18 |
| Mean MAXHT40 (km) | 0.00* | 0.00* | 3.44 | 5.53 | 5.71 | 8.64 | 12.32 | 6.04 |
| Stratiform percentages (%) | 88.63 | 9.46 | 54.38 | 53.22 | 69.90 | 57.42 | 53.02 | 66.83 |
| Convective percentages (%) | 5.85 | 89.95 | 42.83 | 44.52 | 28.16 | 39.91 | 44.06 | 31.56 |
| Land percentages (%) | 21.61 | 6.97 | 27.96 | 42.31 | 15.61 | 65.37 | 80.98 | 10.45 |
| Ocean percentages (%) | 78.39 | 93.03 | 72.04 | 57.69 | 84.39 | 34.63 | 19.02 | 89.55 |
| Mean precipitation (mm $h^{-1}$) | 1.60 | 2.35 | 6.21 | 35.94 | 156.67 | 135.46 | 156.37 | 178.30 |
| precipitation Standard deviation (mm $h^{-1}$) | 1.63 | 1.92 | 8.89 | 50.44 | 98.44 | 106.95 | 103.50 | 98.61 |
| Number of samples | 4,184,547 | 3,083,077 | 1,383,261 | 215,611 | 34,982 | 19,790 | 2,096 | 943 |
| Mean precipitation area ($km^2$) | 610.57 | 239.23 | 2761.46 | 7009.37 | 37076.93 | 18485.91 | 22521.51 | 36044.11 |
| >273.15 K frequency (%) | 86.60 | 99.16 | 99.83 | 99.97 | 99.97 | 99.99 | 99.99 | 100.00 |
| 2.5 km Mean MAX-log10($N_w$) [$m^{-3}$ $mm^{-1}$] | 3.47 | 3.70 | 4.06 | 4.49 | 5.20 | 4.72 | 4.88 | 6.07 |
| 2.5 km Mean MAX-$D_m$ [mm] | 1.03 | 1.17 | 2.26 | 2.82 | 2.71 | 3.04 | 3.11 | 2.61 |
| 2.5 km Mean log10($N_w$) [$m^{-3}$ $mm^{-1}$] | 3.23 | 3.45 | 3.36 | 3.39 | 3.83 | 3.36 | 3.35 | 4.45 |
| 2.5 km Mean $D_m$ [mm] | 0.85 | 0.89 | 1.36 | 1.50 | 1.30 | 1.61 | 1.71 | 1.32 |

### 3.2. Global distributions of microphysical features

Fig. 2 and Fig. 3 show the global distributions of the microphysical parameters for the eight types of PSs. To avoid the influence of ground clutter, in each PS, the mean $D_m$ and $N_w$ values at 2.5 km above the ground surface were analyzed. Notably, there was a significant degree of spatial heterogeneity in each panel. The general conclusion is that continental PSs exhibit a higher

$D_m$ than do oceanic PSs. Usually, continental rainfall is associated with high convective activity in which clouds produce large raindrops. In contrast, oceanic rainfall is accompanied by the formation of weak updrafts and the development of a low melting layer, which impedes the formation of large raindrops and results in a high concentration of small raindrops (Saha et al., 2022; Seela et al., 2018). Moreover, $D_m$ decreases with increasing latitude, a trend that is especially notable in high-latitude marine regions (refer to Fig. S2c in the Supplementary Material). Cha et al. (2021) noted that snow primarily comprises small particles (diameter < 1 mm). In high-latitude shallow PS, snowfall may become more frequent from the middle to high latitudes, which can result in a decrease in $D_m$. Notably, the height and thickness of the melting layer may influence raindrop growth (Hu et al., 2024). With increasing latitude, the melting layer becomes thinner, thus reducing the conditions necessary for raindrop growth, which may lead to the formation of a larger number of small raindrops. In the oceanic regions within subtropical shallow PS, the higher sea surface temperature in the tropics is more conducive to convection formation and development. Moreover, $D_m$ varies among the eight clusters in a specific region. For example, in the Amazon region, moderate PS exhibits a lower $D_m$ than deep PS does.

Similar to $D_m$, there is a distinct contrast in $N_w$ between continents and oceans (Das and Chatterjee, 2018). Continental rainfall is usually associated with the cold rain mechanism, whereby raindrops grow as ice particles (Gupta et al., 2023). In contrast, oceanic rainfall is associated with a warm rain regime, in which raindrops grow via a collision-agglomeration mechanism. Consequently, $N_w$ over land is less than that over oceans (Suh et al., 2016). For the same PS, $N_w$ is high in areas with small $D_m$ values and conversely low in areas with large $D_m$ values. For example, in extreme deep PS, the $D_m$ value over the eastern near-equatorial Pacific Ocean, which reaches approximately 1.18 mm, is smaller than that of the other oceanic regions. However, $N_w$ is significantly greater than those in the other regions. In strong PS, the $D_m$ values in near-equatorial Africa and the eastern United States are greater than those in other regions, but the $N_w$ values are lower than those in other regions. It is possible that $D_m$ and $N_w$ may be negatively correlated for the same PS.

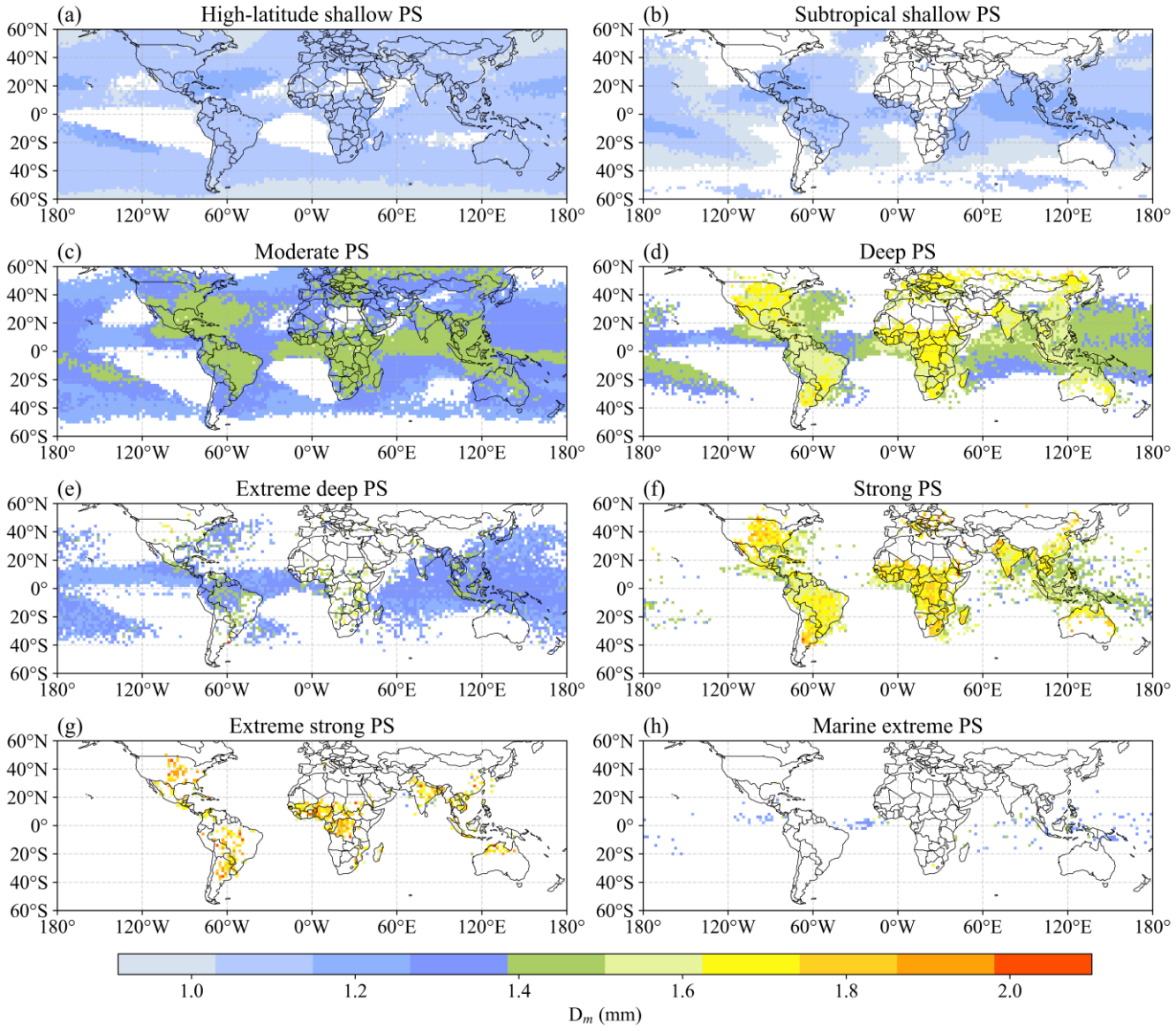


**Figure 2.** Spatial distributions of the mass-weighted mean diameter ($D_m$) for the eight PS clusters at a height of 2.5 km.

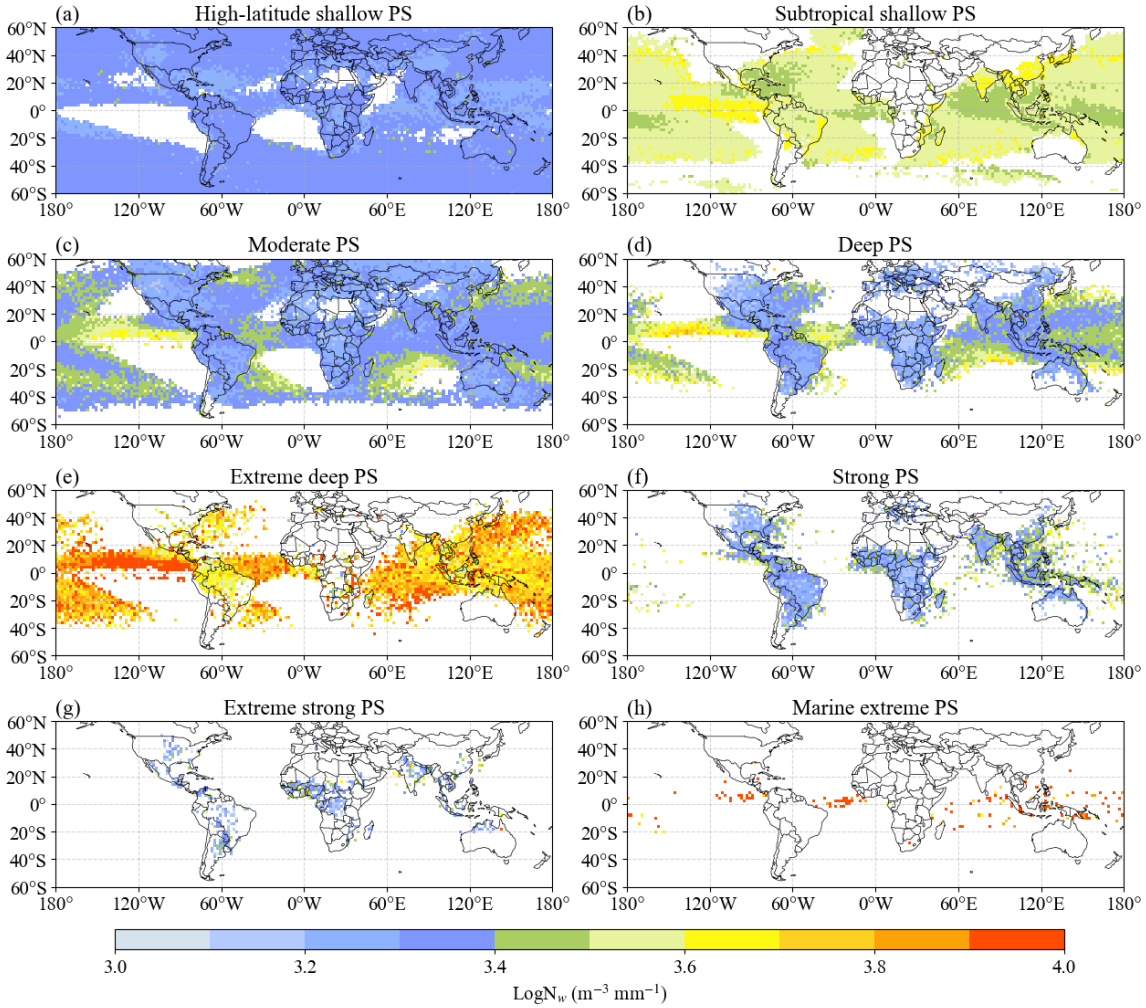


**Figure 3.** Similar to Fig. 2**.** but for log10($N_w$).

### 3.3. Vertical structure of the different PS types

The contoured frequency by altitude diagrams (CFADs) of $D_{m,}$ $N_w$, and the maximum radar reflectivity for the eight clusters are shown in Fig. 4/5/6. Figure 4 shows the CFAD of the maximum radar reflectivity profiles. The results revealed high echo tops for deep PS, extreme deep PS, strong PS, and extreme strong PS, and low echo tops for high-latitude shallow PS and subtropical shallow PS. Extreme strong PS attained an echo top height greater than 18 km, and it also exhibited the strongest convection at the middle level. Its geographic distribution was exclusively terrestrial, which is consistent with other studies concluding that deep convective cores occur mostly over land (Houze Jr. et al., 2015). Extreme deep PS and marine extreme PS exhibited sharper decreasing trends from 6–12 km than extreme strong PS, indicating weaker convective updrafts. In contrast, extreme strong PS had stronger updrafts, producing more supercooled liquid droplets and large ice–water vapor

condensates (Jiang, 2012). In contrast, extreme deep PS and marine extreme PS showed lower 40 dBZ echo tops and a more rapid decrease in reflectivity above the freezing level. This suggests relatively weaker mid- and upper-level updrafts, which limit the vertical transport of ice particles and reduce the abundance of supercooled liquid and large condensate.

Table 1 indicates that the land proportion of extreme strong PS was much greater than that of extreme deep PS and marine extreme PS. Additionally, land indicates a dry adiabatic lapse rate, which results in greater buoyancy and allows for stronger updrafts to lift ice crystals higher into the atmosphere. As a result, the maximum radar reflectivity in the middle levels at high altitudes decreased more slowly in extreme strong PS. High-latitude shallow PS and subtropical shallow PS yielded low echo tops of less than 6 km, indicating low convective intensity. Therefore, subtropical shallow PS could be identified as being associated with isolated shallow convection over the ocean, especially the region dominated by the subtropical high.

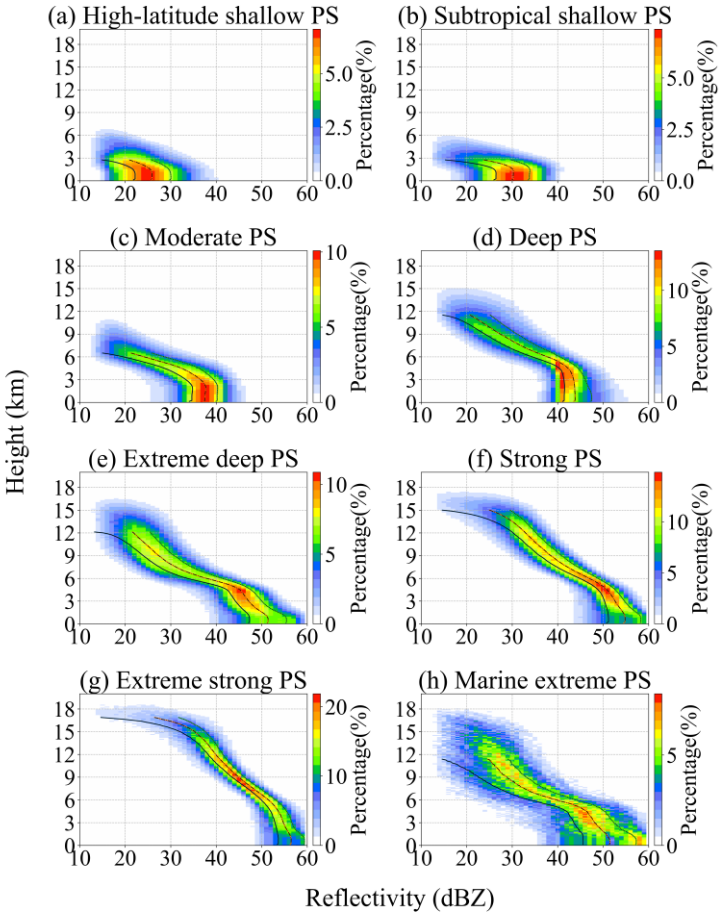

**Figure 4.** Contoured frequency by altitude diagrams (CFADs) of the maximum radar reflectivity for the eight distinct PS clusters. The solid lines indicate the 25th percentiles; the dashed-dotted lines indicate the 50th percentiles; the dotted lines indicate the 75th percentiles.

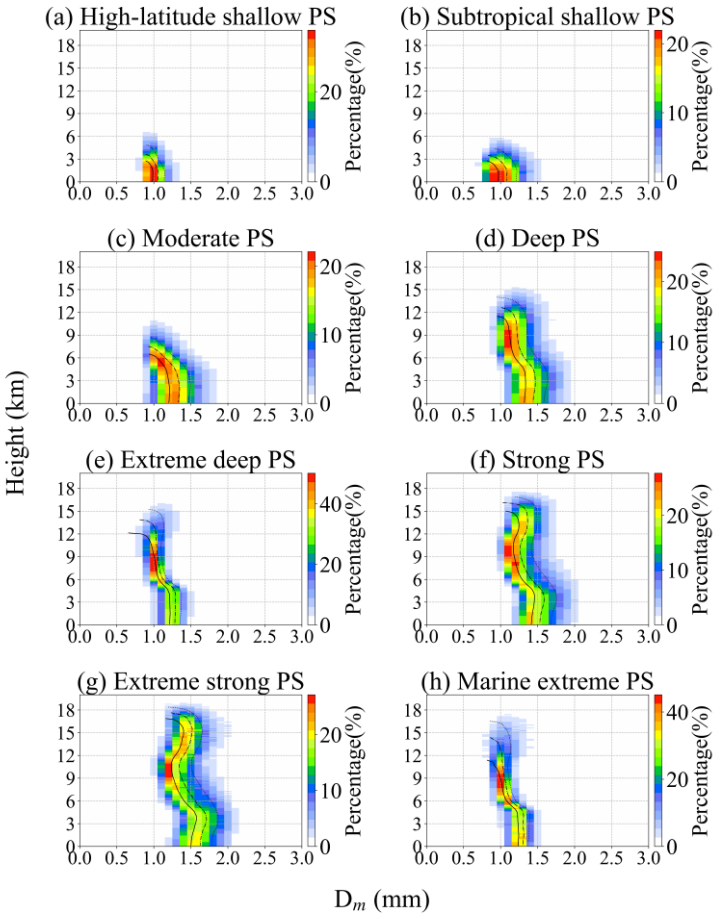


**Figure. 5.** Similar to Fig. 4, but for $D_m$.

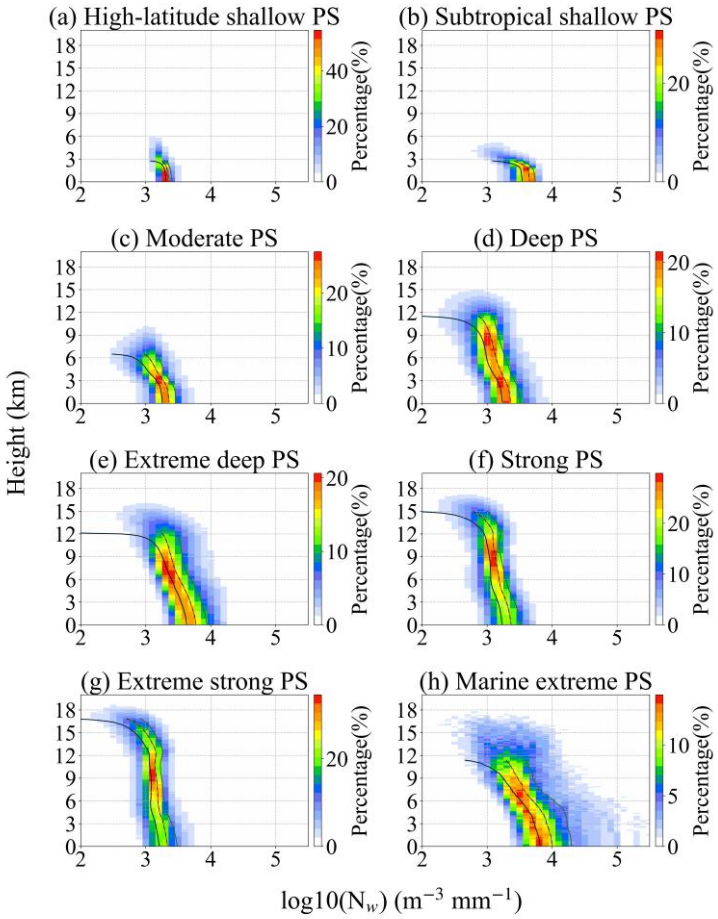


**Figure. 6.** Similar to Fig. 4, but for log10($N_w$).

Figure 5 shows the CFAD of $D_m$ for the eight types of PSs. Generally, deep convections (deep PS, extreme deep PS, strong PS, extreme strong PS, and marine extreme PS) produce different $D_m$ values in the regions above and below approximately 5 km. Moreover, strong PS and extreme strong PS exhibited wider distributions than those of extreme deep PS and marine extreme PS. For deep PS, strong PS, and extreme strong PS, $D_m$ below 4.8 km did not change much or slightly increased along with height, but the value decreased between 4.8 and 6.9 km. In extreme strong PS, the vertical structure of $D_m$ was more complex. Extreme strong PS exhibited three regimes according to the variations in $D_m$. The first regime was observed between 0 and 4.1 km, where $D_m$ increases with altitude. This is consistent with other papers involving the use of ground-based radar observations and reporting that $D_m$ of deep convective precipitation decreases with decreasing height near the surface (Marzuki et al., 2023). The observed decrease in $D_m$ may be related to the continued breakdown of large isolated raindrops in the

atmosphere. The second regime was observed above the freezing level, from 4.1 to 10 km, where $D_m$ decreases with altitude. In this regime, the updraft in deep convection was decreased (Uma and Rao, 2009). The decline in updraft decreased the size of the particles that can be retained in the cloud. The rapid changes of $D_m$ between the two regimes might be due to the changes of precipitation phase across the melting layer. As revealed by Mroz et al. (2024), the routinely retrieval algorithm results in rapid changes of $D_m$ and mass flux around the melting level, because the DPR observations cannot quantify ice particle content and their size above the stratiform rain regions. Finally, the third regime was observed between 10 and 18 km, where $D_m$ increases with altitude and where strengthened updrafts are often observed (Becker and Hohenegger, 2021). Although both high-latitude shallow PS and subtropical shallow PS were shallow PSs, subtropical shallow PS had a wider distribution of $D_m$ than high-latitude shallow PS. One possible reason is that in shallow oceanic convection, the breaking of large raindrops broadens the DSD.

Figure 6 shows the CFAD of log10($N_w$) for the different types of PSs. In general, $N_w$ decreases with increasing altitude. The distribution range of $N_w$ for shallow PSs was relatively small. Moreover, the $N_w$ distribution range of subtropical shallow PS was larger than that of high-latitude shallow PS. Among PSs with intense convection, PSs with a greater proportion of land coverage exhibited more concentrated $N_w$ values, whereas PSs with a greater proportion of ocean coverage exhibited higher $N_w$ values. For example, the $N_w$ values of strong PS and extreme strong PS were smaller and narrower than those of ocean-dominated deep PS, extreme deep PS and marine extreme PS. This finding is consistent with the conclusions of other studies (Kumar et al., 2024). One possible explanation is that the slower updrafts over ocean regions result in higher concentrations of smaller condensates at lower altitudes. Moreover, for both $D_m$ and $N_w$, the four non-extreme PSs exhibit little vertical variation below the melting layer, which may be attributed to a balance between coalescence and breakup processes.

### 3.4. DSD characteristics at a height of 2.5 km

Figure 7a-h show the frequency distributions of the mean $D_m$ and log10($N_w$) values observed at 2.5 km above ground level. The mean $D_m$ values and the corresponding log10($N_w$) values for the eight types of PSs are detailed in Table 1. Generally, all the distributions shown in Fig. 7a-h greatly deviate from the parameters of continental convection and maritime convection defined by Bringi et al. (2003). One reason is that the mean values of $D_m$ and $N_w$ for one PS were considered here, whereas Bringi et al. (2003) separated the observation samples into stratiform and convection samples. Moreover, the DSDs observed by disdrometers are generally cumulative observations of a single storm at one fixed location and differ from the results for each PS in this study, which represent the instantaneous occurrence of a storm. With the most intense convection at the middle level, extreme strong PS was the closest to continental convection (Fig. 7d), whereas marine extreme PS was the closest to maritime convection (Fig. 7e). For most PSs, $D_m$ and $N_w$ were negatively correlated, with greater dispersion of $D_m$ than that of $N_w$. However, it should be noted that the observed correlations between $D_m$ and $N_w$ may partly be due to the retrieval assumptions in the GPM algorithm, which enforces a correlation between $D_m$ and precipitation rate (Chase et al., 2020), rather

than purely physical relationships. Moreover, the shallow PSs exhibited lower $D_m$ and $N_w$ values and more concentrated distributions than those of the deep PSs.

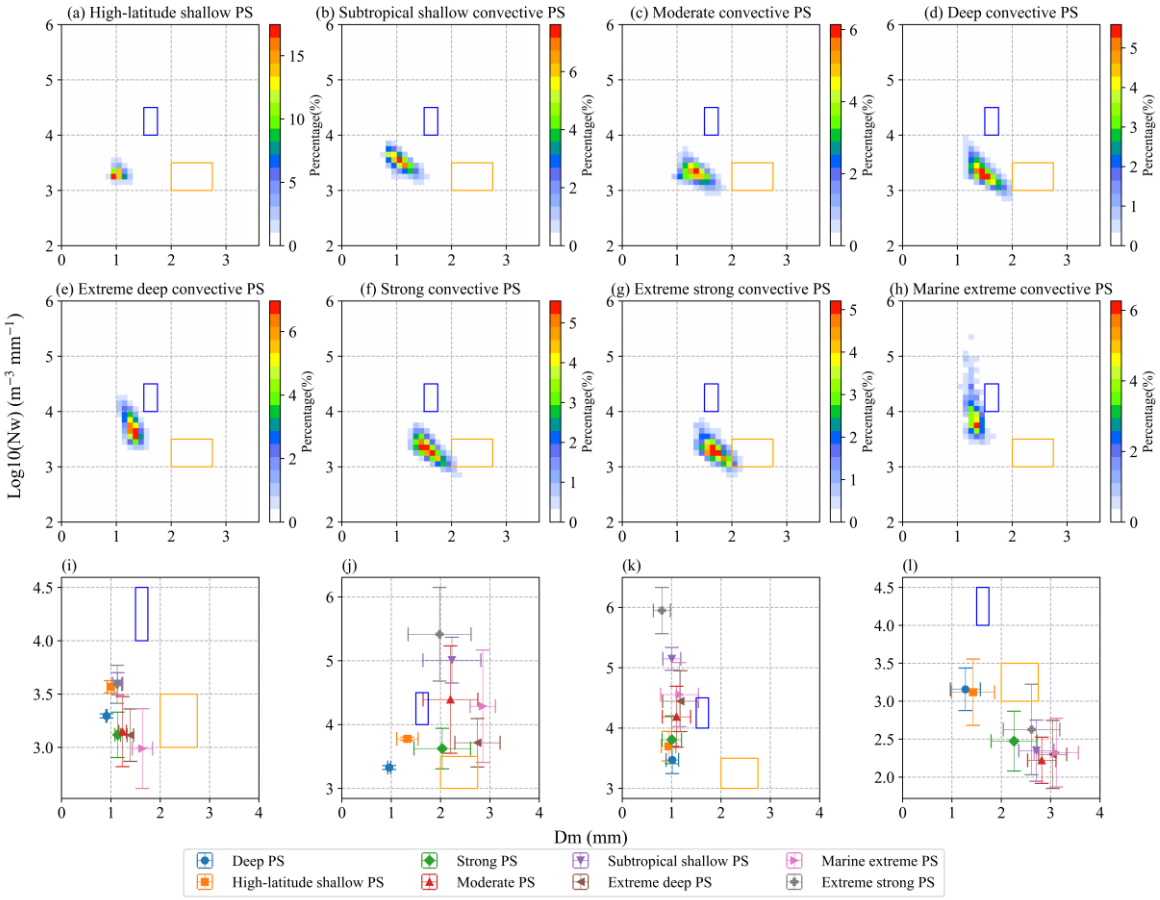


**Figure 7.** (a-h) Two-dimensional frequency distributions of $D_m$ and log10($N_w$) at a height of 2.5 km, and (i-l) statistical values of log10($N_w$) and $D_m$ for each PS (the bar indicates one standard deviation). (i) Mean values of $D_m$ and log10($N_w$), (j) MAX-$D_m$ and MAX-log10($N_w$), (k) MAX-log10($N_w$) and $D_m$ at its corresponding position, and (l) MAX-$D_m$ and log10($N_w$) at its corresponding position for each PS. (the blue and orange rectangles denote the maritime and continental convective clusters, respectively, in $D_m$ and log10($N_w$) space from Bringi et al. (2003)).

To further compare the mean $D_m$ and $N_w$ values of the different clusters, Figure 7i shows a summary of the mean $D_m$ and $N_w$ values, with the standard deviation for each type of PS. Marine extreme PS showed a significant abnormal value of $N_w$, whereas the $N_w$ value of extreme deep PS slightly deviated from those of the other PS. If only the three extreme deep PSs with the highest echo tops (strong, extreme strong, and marine extreme PS) are considered, $D_m$ and $N_w$ show an inverse relationship.

These results might suggest that in deep convection, the DSD parameters at the near-surface level are related to convection intensity parameters. Ni et al. ( 2019) revealed that the dual-frequency ratio between the Ku and Ka bands at 12 km was positively correlated with intensity parameters such as MAXHT20/30, partly because stronger updrafts could hold larger ice particles in clouds.

Note that although the mean $D_m$ and $N_w$ values do not capture the variety of DSDs in each PS. For example, the DSD might differ between convective and stratiform regions, where the $N_w$–$D_m$ relationships might vary. To comprehensively demonstrate the microphysical features of PSs, Figure 7j shows the mean MAX-$D_m$ and MAX-$N_w$ values of each PS at 2.5 km. For extreme PS, MAX-$D_m$ and MAX-$N_w$ were negatively correlated, while a positive correlation was observed for non-extreme PS. A similar relationship is also shown in Fig. 7k, which suggests a relationship between MAX-$N_w$ and the corresponding $D_m$ value in the MAX-$N_w$ pixels of each PS. Nevertheless, as shown in Fig. 7k, the $D_m$ values of all eight types of PSs were very close. Nevertheless, it could be also found that in the non-extreme PS the $D_m$ increases with MAX-$N_w$, while in the extreme PS, the $D_m$ decreases with MAX-$N_w$. Figure 7l shows the relationship between MAX-$D_m$ and the corresponding $N_w$ value in the MAX-$D_m$ pixels of each PS. Interestingly, for all eight types of PSs, MAX-$D_m$ and $N_w$ showed significantly negative correlations. Note that MAX-$D_m$ and MAX-$N_w$ in Fig. 7j are the maximum values for one PS and usually do not occur in the same pixel. Figure 7k-l show the $N_w$–$D_m$ relationship observed at the same location. Overall, the conclusions generally indicated that deep PSs yield larger MAX-$N_w$ or MAX-$D_m$ values than shallow convection PSs do. Overall, extreme PS exhibited negative correlations between $N_w$ and $D_m$, whereas non-extreme PS demonstrated positive correlations.

Ryu et al. (2021) analyzed DSDs during three types of heavy rainfall events with different rain intensities. They also reported that $D_m$ increases with increasing rainfall intensity, whereas $N_w$ decreases with increasing rainfall intensity. In this study, we saw a positive relationship between the increase in $D_m$ and MAXHT20 in extreme PS. However, extreme strong PS attained the highest MAXHT20 value, but its precipitation rate was lower than that of extreme deep PS and marine extreme PS. These results suggest a complex relationship between the microphysical parameters and convection features, especially in deep and intense convection systems. Notably, in extreme convection, with strong convection at the top of the storm, attenuation becomes notable at low storm levels, which might influence the retrieval of microphysical parameters. To assess the impact of attenuation on the $D_m$-$N_w$ relationship, ground-based observations of microphysical properties from disdrometers are needed. Finally, we considered the PS as a whole. The microphysical characteristics varied among different pixels. The mean or maximum values of $D_m$ and $N_w$ only reflect part of the total process. Therefore, analyses on the basis of pixel-level observations would improve this work.

To gain further insight into the primary microphysical processes associated with the various PS, we employed an investigative approach analogous to that utilized by Kumjian and Prat (2014). To prevent the influence of ground-based clutter, $\Delta Z_e$ and $\Delta D_m$ values were calculated as the difference between $Z_e$ and $D_m$ at 2 and 3 km above the ground. Specifically, $\Delta Z_e = Z_e^{2km}$ -

$Z_e^{3km}$ and $\Delta D_m = D_m^{2km} - D_m^{3km}$ are calculated. Fig. 8 shows the frequency pattern of $\Delta Z_e$ versus $\Delta D_m$ for the eight types of PSs. An increase (decrease) in $Z_e$ and $D_m$ indicates that coalescence (breakup) processes dominate. Balanced breakup and coalescence processes result in an increase in $Z_e$ but a decrease in $D_m$. In contrast, a decrease in $Z_e$ and an increase in $D_m$ are due to predominate evaporation or size sorting processes (Wen et al., 2023).

The microphysical processes of the different types of PSs were significantly distinct. Notably, the microphysical processes were dominated by coalescence in the two types of shallow PS (Fig. 8a-b). Previous studies have demonstrated that high-latitude shallow PS are more likely to experience the condensation of rain droplets into snow due to the low temperatures in these regions (Thompson et al., 2015). Meanwhile, the coalescence process plays an important role in tropical oceanic shallow convective precipitation (subtropical shallow PS) as demonstrated by Li et al. (2024). Balanced breakup and coalescence processes in the microphysical processes of extreme PS accounted for more than 40% of the total microphysical processes, significantly exceeding other three types of microphysical processes. The microphysical processes may reach an equilibrium state under high rainfall rates, in which the coalescence and breakup of raindrops are nearly balanced. These results are consistent with Shi et al. (2025), who found that extreme rainfall is primarily driven by vigorous mixed-phase processes and a balance between coalescence and breakup in liquid-phase processes. Extreme deep PS and marine extreme PS encompassed a higher percentage of coalescence processes than strong PS and extreme strong PS did, whereas strong PS and extreme strong PS encompassed a higher percentage of breakup processes.

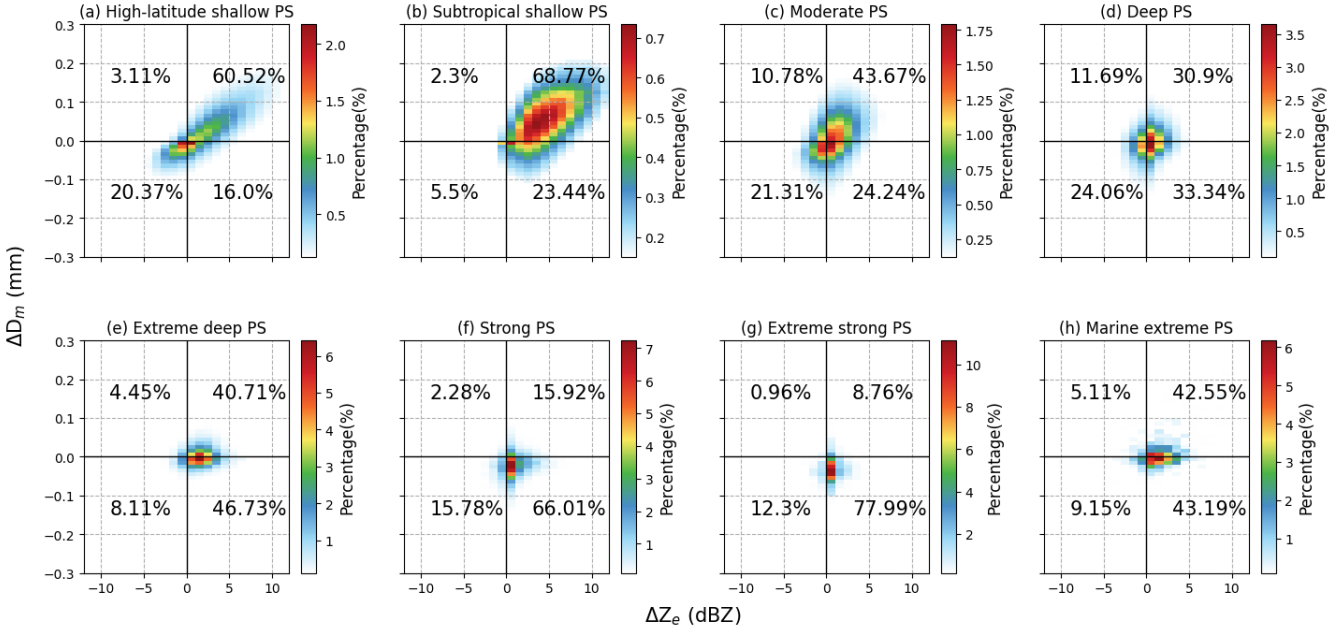


**Figure 8.** Frequency pattern of $\Delta Z_e$ versus $\Delta D_m$ between 2 and 3 km for the eight PS clusters.

### 3.5. Seasonal and diurnal cycles

In this study, seasons were categorized by fixed calendar months. The Northern Hemisphere seasons were defined as spring (March–May), summer (June–August), autumn (September–November), and winter (December–February). Conversely, the Southern Hemisphere seasons followed the opposite pattern: spring (September–November), summer (December–February), autumn (March–May), and winter (June–August). Based on this classification, the subsequent analysis examines seasonal and diurnal variations in PS frequency and microphysical parameters. Figure 9 shows the cycles of PS occurrence. Overall, the seasonal and diurnal cycles differed among the eight types of PSs. Moderate PS, deep PS, strong PS, and extreme strong PS exhibited cycles like those of continental convection systems, with peaks in the afternoon and in summer. Dominated by tropical shallow convection over the ocean (Fig. 1**)**, subtropical shallow PS occurred mostly between 0 and 5 a.m. and was more frequent during the autumn season than during the other seasons, with the lowest occurrence during the spring season. The other types of PS (high-latitude shallow PS, extreme deep PS, and marine extreme PS) did not show obvious diurnal cycles, except that high-latitude shallow PS indicated a low peak at approximately 6 am in winter and a valley before noon in summer. High-latitude shallow PS occurred infrequently in winter. Extreme deep PS occurred more frequently in summer and autumn, with fewer occurrences in winter. Note that marine extreme PS did not demonstrate obvious seasonal discrepancies, but shown a peak at night in the summer. Specifically, strong PS and extreme strong PS with a higher proportion over land exhibit a peak occurrence around 3 p.m. in the afternoon. In contrast, extreme deep PS and marine extreme PS mostly show no distinct peak, with frequencies distributed evenly throughout the day. This difference reflects the land-ocean contrast in extreme PS, which is consistent with findings from other related studies (Wang and Tang, 2020).

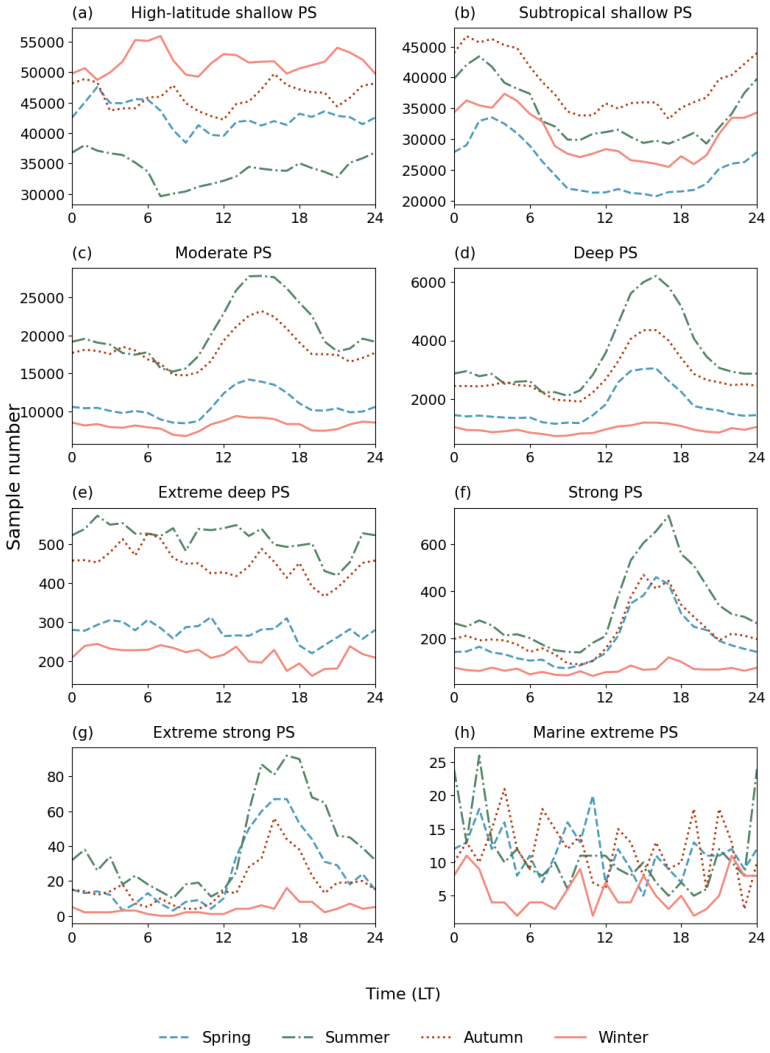


460

461 **Figure 9.** Diurnal variations in the sample sizes of the eight distinct PS clusters across the four seasons.

462 Figures 10 and 11 show the seasonal and diurnal cycles of $D_m$ and $N_w$, respectively. The diurnal cycles of $D_m$ were similar
463 with those of PS occurrence to some extent. For example, in moderate PS, deep PS and strong PS, both the occurrence and $D_m$
464 have peaks in the around 15 pm. One connection between these two parameters is that environments that favor storm
465 occurrence could also facilitate the development of stronger updrafts, which could promote the formation of large particles in
466 clouds. Nevertheless, discrepancies are obvious between the cycles of occurrence and $D_m$. For example, the $D_m$ in the extreme
467 strong PS did not show obvious diurnal variations. The high-latitude shallow PS shows a peak in the summer (Fig. 10a), which
468 is not found in the diurnal cycle of occurrence (Fig. 9a). In subtropical shallow PS, the diurnal cycle of $D_m$ (Fig. 10b) was the
469 opposite to that of PS occurrence (Fig. 9b). The diurnal cycles of $N_w$ were basically different with those of $D_m$ and occurrence.
470 In subtropical shallow PS, moderate PS, deep PS, and strong PS, the $N_w$ peaked in the morning. Nevertheless, the diurnal

cycles of subtropical shallow PS, moderate PS, and deep PS also differed. For example, $N_w$ of subtropical shallow PS at night was low, whereas $N_w$ of shallow convective PS and moderate PS at night was very close to its peak. Extreme deep PS and marine extreme PS did not exhibit obvious diurnal cycles of $N_w$. The extreme strong PS shown low values of $N_w$ in the afternoon and little variations at night. For high-latitude shallow PS, diurnal variation is not clear except in the summer when the $N_w$ in the afternoon is the lowest.

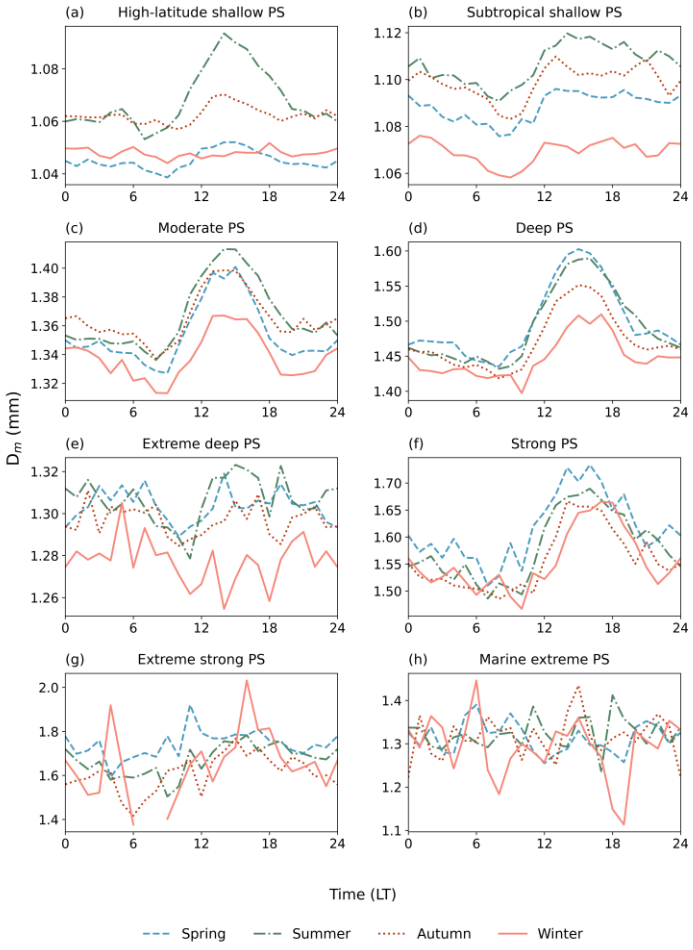


**Figure 10.** Similar to Fig. 9 but for mean $D_m$ value.

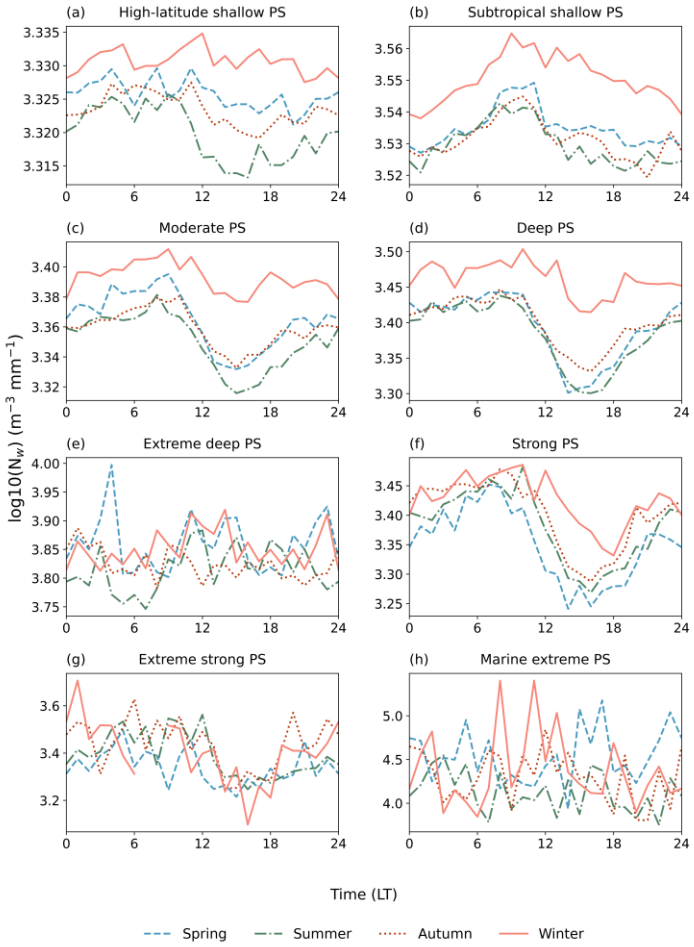


**Figure 11.** Similar to Fig. 9 but for the mean log10($N_w$) value.

Similar to the diurnal cycles, the annual cycles of $D_m$ and $N_w$ were opposite in subtropical shallow PS, moderate PS, and deep PS, of which $D_m$ was the lowest and $N_w$ was the largest in winter. Nevertheless, there were also differences in the annual cycles of the three types of PSs. For example, in subtropical shallow PS, $D_m$ was the largest in summer, followed by autumn and spring, whereas the $N_w$ values during the three seasons were very close. Among the extreme PS, $N_w$ and $D_m$ did not exhibit obvious annual cycles. For high-latitude shallow PS, the highest $D_m$ value occurs in summer and the $D_m$ in winter and spring were comparable. However, the annual cycle of $N_w$ attained the largest value in winter and the lowest value in summer.

## 4. Conclusions

In this study, GPM DPR data were used to objectively classify global PS and analyze the microphysical characteristics of the different types of PS. The main conclusions are as follows:

1). By conducting an objective classification of global PSs via key parameters such as the convective intensity, radar reflectivity, and DSD parameters, eight distinct types of PSs were identified. These systems were classified on the basis of their unique microphysical and convection properties, providing a detailed understanding of the different precipitation processes worldwide. The eight types of PSs identified are as four types of regular/non-extreme PS (high-latitude shallow PS, subtropical shallow PS, moderate PS, deep PS) and four types of extreme PS (extreme deep PS, strong PS, extreme strong PS, marine extreme PS).

2). MAXHT20 is generally correlated with the precipitation rate, but this relationship is not clear for extreme PS. The relationship between MAXHT20 and $D_m$ does not follow a simple linear pattern. For extreme PS, MAXHT20 is positively related to $D_m$ at 2.5 km above the ground surface. This may reflect the relationship between higher cloud tops and greater liquid water contents in strongly convective PSs. However, for non-extreme PS, the relationship between MAXHT20 and $D_m$ is more complex and may be influenced by variations in the physical processes of the different PS.

3). For the same type of PS, $D_m$ over land is greater than that over the ocean. Additionally, $D_m$ exhibits latitudinal variability, particularly in high-latitude shallow PS, where $D_m$ decreases with increasing latitude. Additionally, continental rainfall is associated with lower $N_w$ values due to the cold rain mechanism, whereas oceanic rainfall is associated with higher $N_w$ values resulting from a warm rain regime. Shallow PS generally exhibit narrow distributions of both $D_m$ and $N_w$, particularly in high-latitude shallow PS. Among the strong PS, PS with a higher land proportion exhibit more concentrated $N_w$ values, whereas those with a greater ocean proportion exhibit larger $N_w$ values. However, the distribution of $D_m$ is the opposite: PS with a higher ocean proportion exhibit more concentrated $D_m$ values than land-dominated PSs do.

4). The different PS exhibit distinct microphysical processes. In shallow convective PS, such as subtropical shallow PS and high-latitude shallow PS, coalescence processes largely shape the microphysical characteristics, indicating the aggregation of small raindrops in these PS. In contrast, extreme PSs are characterized by balanced breakup and coalescence processes, highlighting a more complex interaction between raindrop formation and breakup. These results emphasize the varying mechanisms that govern microphysical behavior across the different types of PSs. PS types with high precipitation rates are dominated primarily by balanced breakup and coalescence processes, whereas shallow PSs are characterized mainly by coalescence.

5). The seasonal and diurnal cycles of PSs and their microphysical parameters vary across clusters. Continental convection Cluster peak in the afternoon and summer, whereas tropical and high-latitude systems exhibit unique seasonal and diurnal cycles, often with opposite trends between $D_m$ and $N_w$.

Classifying PS is essential for increasing the understanding of the microphysical processes that govern cloud development and precipitation formation across various climatic regimes. This classification enables the identification of specific mechanisms that influence rainfall characteristics, such as droplet formation, growth, and distribution, which are vital for accurate weather predictions and climate modeling. This study revealed the global distribution characteristics of different types of PS and elucidated the variations in microphysical properties across regions with distinct climatic and geographic conditions.

In this study, each PS was treated as integrated entity, without considering the variations in $D_m$ and $N_w$ within each system. Microphysical properties can vary significantly at the pixel level, and relying solely on average or maximum $D_m$ and $N_w$ values captures only part of the overall process. Future work should focus on analyzing pixel-level observations to better understand the characteristics of microphysical parameters within PS. Moreover, the melting layer height was not explicitly considered, which limits the interpretation of vertical variations across the melting layer. Future work should incorporate pixel-level observations and melting layer characteristics to better understand the microphysical features within PSs. Furthermore, investigating the relationships between microphysical parameters and convective parameters will be a key focus of future research. It should also be noted that the DPR is not particularly suitable for quantifying extreme precipitation rates. In heavy precipitation, Ku- and Ka-band signals are strongly affected by attenuation and multiple scattering, which can lead to underestimation of radar reflectivity and the associated precipitation rates (Battaglia et al., 2014). Therefore, no further discussion of extreme rain rates is provided in this study. We hope that future studies can develop improved precipitation retrieval algorithms to address this issue. By analyzing the interactions between these parameters, it is possible to reveal the influences of microphysical characteristics on convective intensity and precipitation patterns, providing a more detailed perspective for accurately predicting and understanding precipitation phenomena.

**Data Availability.** The GPM-DPR (version 07A) data from the NASA/G-oddard Space Flight Center are available at https://disc.gsfc.nasa.gov/datasets/GPM_2A-DPR_07/summary. All statistics and visualization are operated with Anaconda Individual Edition Python version 3.8.3 (Free Download | Anaconda, accessed on 10 April 2022).

**Author contributions.** XZ and XN conceptualised and planned the research study. XZ conducted the satellite data analysis with support from XN and drafted the initial manuscript. XN and JZ reviewed and revised the manuscript to refine its content.

**Competing interests.** The contact author has declared that none of the authors has any competing interests.

**Financial support.** This study is supported by the National Natural Science Foundation of China (42105005), Fundamental Research Funds for the Central Universities (SWU-KT22007), and General Program of Chongqing Natural Science Foundation (2022NSCQ-MSX3145).

## References

Arulraj, M. and Barros, A. P.: Automatic detection and classification of low-level orographic precipitation processes from space-borne radars using machine learning, Remote Sensing of Environment, 257, 112355, https://doi.org/10.1016/j.rse.2021.112355, 2021.

Awaka, J., Le, M., Brodzik, S., Kubota, T., Masaki, T., Chandrasekar, V., and Iguchi, T.: Development of precipitation type classification algorithms for a full scan mode of GPM dual-frequency precipitation radar, Journal of the Meteorological Society of Japan. Ser. II, 99, 1253–1270, https://doi.org/10.2151/jmsj.2021-061, 2021.

Ay, M., Özbakır, L., Kulluk, S., Gülmez, B., Öztürk, G., and Özer, S.: FC-Kmeans: Fixed-centered K-means algorithm, Expert Systems with Applications, 211, 118656, https://doi.org/10.1016/j.eswa.2022.118656, 2023.

Bang, S. D. and Cecil, D. J.: Testing Passive Microwave-Based Hail Retrievals Using GPM DPR Ku-Band Radar, Journal of Applied Meteorology and Climatology, 60, 255–271, https://doi.org/10.1175/JAMC-D-20-0129.1, 2021.

Battaglia, A., Tanelli, S., Heymsfield, G. M., and Tian, L.: The Dual Wavelength Ratio Knee: A Signature of Multiple Scattering in Airborne Ku–Ka Observations, Journal of Applied Meteorology and Climatology, 53, 1790–1808, https://doi.org/10.1175/JAMC-D-13-0341.1, 2014.

Becker, T. and Hohenegger, C.: Entrainment and its dependency on environmental conditions and convective organization in convection-permitting simulations, Monthly Weather Review, 149, 537–550, https://doi.org/10.1175/MWR-D-20-0229.1, 2021.

Bringi, V. N., Chandrasekar, V., Hubbert, J., Gorgucci, E., Randeu, W. L., and Schoenhuber, M.: Raindrop size distribution in different climatic regimes from disdrometer and dual-polarized radar analysis, Journal of the Atmospheric Sciences, 60, 354–365, https://doi.org/10.1175/1520-0469(2003)060<0354:RSDIDC>2.0.CO;2, 2003.

Cha, J. W. and Yum, S. S.: Characteristics of Precipitation Particles Measured by PARSIVEL Disdrometer at a Mountain and a Coastal Site in Korea, Asia-Pacific J Atmos Sci, 57, 261–276, https://doi.org/10.1007/s13143-020-00190-6, 2021.

Chase, R. J., Nesbitt, S. W., and McFarquhar, G. M.: Evaluation of the Microphysical Assumptions within GPM-DPR Using Ground-Based Observations of Rain and Snow, Atmosphere, 11, 619, https://doi.org/10.3390/atmos11060619, 2020.

Chen, B. and Liu, C.: Warm organized rain systems over the tropical eastern Pacific, Journal of Climate, 29, 3403–3422, https://doi.org/10.1175/JCLI-D-15-0177.1, 2016.

Chen, B., Hu, W., and Pu, J.: Characteristics of the raindrop size distribution for freezing precipitation observed in southern China, Journal of Geophysical Research: Atmospheres, 116, https://doi.org/10.1029/2010JD015305, 2011.

Chudler, K., Rutledge, S. A., and Dolan, B.: Unique radar observations of large raindrops in tropical warm rain during PISTON, Monthly Weather Review, 150, 2719–2736, https://doi.org/10.1175/MWR-D-21-0298.1, 2022.

D'Adderio, L. P., Vulpiani, G., Porcù, F., Tokay, A., and Meneghini, R.: Comparison of GPM Core Observatory and Ground-Based Radar Retrieval of Mass-Weighted Mean Raindrop Diameter at Midlatitude, Journal of Hydrometeorology, 19, 1583–1598, https://doi.org/10.1175/JHM-D-18-0002.1, 2018.

Dai, Q., Zhu, J., Zhang, S., Zhu, S., Han, D., and Lv, G.: Estimation of rainfall erosivity based on WRF-derived raindrop size distributions, Hydrology and Earth System Sciences, 24, 5407–5422, https://doi.org/10.5194/hess-24-5407-2020, 2020.

Das, S. and Chatterjee, C.: Rain characterization based on maritime and continental origin at a tropical location, Journal of Atmospheric and Solar-Terrestrial Physics, 173, 109–118, https://doi.org/10.1016/j.jastp.2018.02.011, 2018.

Das, S., Wang, Y., Gong, J., Ding, L., Munchak, S. J., Wang, C., Wu, D. L., Liao, L., Olson, W. S., and Barahona, D. O.: A comprehensive machine learning study to classify precipitation type over land from Global Precipitation Measurement Microwave Imager (GPM-GMI) measurements, Remote Sensing, 14, 3631, https://doi.org/10.3390/rs14153631, 2022.

Dolan, B., Fuchs, B., Rutledge, S. A., Barnes, E. A., and Thompson, E. J.: Primary modes of global drop size distributions, Journal of the Atmospheric Sciences, 75, 1453–1476, https://doi.org/10.1175/JAS-D-17-0242.1, 2018.

El Khattabi, M.-Z., El Jai, M., Lahmadi, Y., Oughdir, L., and Rahhali, M.: Understanding the Interplay Between Metrics, Normalization Forms, and Data distribution in K-Means Clustering: A Comparative Simulation Study, Arab J Sci Eng, 49, 2987–3007, https://doi.org/10.1007/s13369-023-07741-9, 2024.

Festa, D., Novellino, A., Hussain, E., Bateson, L., Casagli, N., Confuorto, P., Del Soldato, M., and Raspini, F.: Unsupervised detection of InSAR time series patterns based on PCA and K-means clustering, International Journal of Applied Earth Observation and Geoinformation, 118, 103276, https://doi.org/10.1016/j.jag.2023.103276, 2023.

Gang, A. and Bajwa, W. U.: FAST-PCA: A Fast and Exact Algorithm for Distributed Principal Component Analysis, IEEE Transactions on Signal Processing, 70, 6080–6095, https://doi.org/10.1109/TSP.2022.3229635, 2022.

Gupta, A. K., Deshmukh, A., Waman, D., Patade, S., Jadav, A., Phillips, V. T. J., Bansemer, A., Martins, J. A., and Gonçalves, F. L. T.: The microphysics of the warm-rain and ice crystal processes of precipitation in simulated continental convective storms, Commun Earth Environ, 4, 226, https://doi.org/10.1038/s43247-023-00884-5, 2023.

Hamada, A., Takayabu, Y. N., Liu, C., and Zipser, E. J.: Weak linkage between the heaviest rainfall and tallest storms, Nature Communications, 6, 6213, https://doi.org/10.1038/ncomms7213, 2015.

Hou, A. Y., Kakar, R. K., Neeck, S., Azarbarzin, A. A., Kummerow, C. D., Kojima, M., Oki, R., Nakamura, K., and Iguchi, T.: The global precipitation measurement mission, Bulletin of the American Meteorological Society, 95, 701–722, https://doi.org/10.1175/BAMS-D-13-00164.1, 2014.

Houze Jr., R. A., Rasmussen, K. L., Zuluaga, M. D., and Brodzik, S. R.: The variable nature of convection in the tropics and subtropics: A legacy of 16 years of the Tropical Rainfall Measuring Mission satellite, Reviews of Geophysics, 53, 994–1021, https://doi.org/10.1002/2015RG000488, 2015.

Hu, X., Ai, W., Qiao, J., and Yan, W.: Insight into global climatology of melting layer: latitudinal dependence and orographic relief, Theor Appl Climatol, 155, 4863–4873, https://doi.org/10.1007/s00704-024-04926-6, 2024.

Iguchi, T., Kozu, T., Meneghini, R., Awaka, J., and Okamoto, K.: Rain-Profiling algorithm for the TRMM precipitation radar, Journal of Applied Meteorology and Climatology, 39, 2038–2052, https://doi.org/10.1175/1520-0450(2001)040<2038:RPAFTT>2.0.CO;2, 2000.

Iguchi, T., Seto, S., Meneghini, R., Yoshida, N., Awaka, J., Le, M., Chandrasekar, V., Brodzik, S., Tanelli, S., Kanemaru, K., Masaki, T., Kubota, T., and Takahashi, N.: GPM/DPR Level-2 Algorithm Theoretical Basis Document, 2021.

Jain, A. K.: Data clustering: 50 years beyond K-means, Pattern Recognition Letters, 31, 651–666, https://doi.org/10.1016/j.patrec.2009.09.011, 2010.

Jiang, H.: The relationship between tropical cyclone intensity change and the strength of inner-core convection, Monthly Weather Review, 140, 1164–1176, https://doi.org/10.1175/MWR-D-11-00134.1, 2012.

Jolliffe, I. T. and Cadima, J.: Principal component analysis: a review and recent developments, Philosophical Transactions of the Royal Society A: Mathematical, Physical and Engineering Sciences, 374, 20150202, https://doi.org/10.1098/rsta.2015.0202, 2016.

Kumar, K. S., Das, S. K., Deshpande, S. M., Deshpande, M., and Pandithurai, G.: Regional variability of precipitation characteristics in tropical cyclones over the North Indian Ocean from GPM-DPR measurements, Atmospheric Research, 283, 106568, https://doi.org/10.1016/j.atmosres.2022.106568, 2023.

Kumar, S., Flores-Rojas, J. L., Moya-Álvarez, A. S., Martínez-Castro, D., and Silva, Y.: Hydrometeors distribution in intense precipitating cloud cells over the earth's during two rainfall seasons, J Indian Soc Remote Sens, 52, 95–111, https://doi.org/10.1007/s12524-023-01805-x, 2024.

Kumjian, M. R. and Prat, O. P.: The impact of raindrop collisional processes on the polarimetric radar variables, Journal of the Atmospheric Sciences, 71, 3052–3067, https://doi.org/10.1175/JAS-D-13-0357.1, 2014.

Lerber, A. von, Moisseev, D., Marks, D. A., Petersen, W., Harri, A.-M., and Chandrasekar, V.: Validation of GMI Snowfall Observations by Using a Combination of Weather Radar and Surface Measurements, Journal of Applied Meteorology and Climatology, 57, 797–820, https://doi.org/10.1175/JAMC-D-17-0176.1, 2018.

Li, D., Qi, Y., and Li, H.: Statistical characteristics of convective and stratiform precipitation during the rainy season over South China based on GPM-DPR observations, Atmospheric Research, 301, 107267, https://doi.org/10.1016/j.atmosres.2024.107267, 2024.

Liu, C.: Rainfall Contributions from Precipitation Systems with Different Sizes, Convective Intensities, and Durations over the Tropics and Subtropics, Journal of Hydrometeorology, 12, 394–412, https://doi.org/10.1175/2010JHM1320.1, 2011.

Liu, C. and Zipser, E. J.: The global distribution of largest, deepest, and most intense precipitation systems, Geophysical Research Letters, 42, 3591–3595, https://doi.org/10.1002/2015GL063776, 2015.

Liu, C., Zipser, E. J., and Nesbitt, S. W.: Global Distribution of Tropical Deep Convection: Different Perspectives from TRMM Infrared and Radar Data, https://doi.org/10.1175/JCLI4023.1, 2007.

652 Liu, C., Zipser, E. J., Cecil, D. J., Nesbitt, S. W., and Sherwood, S.: A cloud and precipitation feature database from nine years
653 of TRMM observations, Journal of Applied Meteorology and Climatology, 47, 2712–2728,
654 https://doi.org/10.1175/2008JAMC1890.1, 2008.
655 Liu, N., Liu, C., and Hayden, L.: Climatology and detection of overshooting convection from 4 years of GPM precipitation
656 radar and passive microwave observations, Journal of Geophysical Research: Atmospheres, 125, e2019JD032003,
657 https://doi.org/10.1029/2019JD032003, 2020.
658 Marukatat, S.: Tutorial on PCA and approximate PCA and approximate kernel PCA, Artif Intell Rev, 56, 5445–5477,
659 https://doi.org/10.1007/s10462-022-10297-z, 2023.
660 Marzuki, M., Ramadhan, R., Yusnaini, H., Renggono, F., Vonnisa, M., and Hashiguchi, H.: Comparison of vertical profile of
661 raindrop size distribution from micro rain radar with global precipitation measurement over Western Java Island, Remote
662 Sensing Applications: Society and Environment, 29, 100885, https://doi.org/10.1016/j.rsase.2022.100885, 2023.
663 Mroz, K., Battaglia, A., and Fridlind, A. M.: Enhancing consistency of microphysical properties of precipitation across the
664 melting layer in dual-frequency precipitation radar data, Atmospheric Measurement Techniques, 17, 1577–1597,
665 https://doi.org/10.5194/amt-17-1577-2024, 2024.
666 Ni, X., Liu, C., Cecil, D. J., and Zhang, Q.: On the detection of hail Using satellite passive microwave radiometers and
667 precipitation radar, Journal of Applied Meteorology and Climatology, 56, 2693–2709, https://doi.org/10.1175/JAMC-D-17-
668 0065.1, 2017.
669 Ni, X., Liu, C., and Zipser, E.: Ice microphysical properties near the tops of deep convective cores implied by the GPM Dual-
670 Frequency Radar observations, Journal of the Atmospheric Sciences, 76, 2899–2917, https://doi.org/10.1175/JAS-D-18-
671 0243.1, 2019.
672 Peinó, E., Bech, J., Polls, F., Udina, M., Petracca, M., Adirosi, E., Gonzalez, S., and Boudevillain, B.: Validation of GPM DPR
673 Rainfall and Drop Size Distributions Using Disdrometer Observations in the Western Mediterranean, Remote Sensing, 16,
674 2594, https://doi.org/10.3390/rs16142594, 2024.
675 Roy, P., Biswasharma, R., Deshamukhya, A., and Sharma, S.: Spatial and seasonal variation of rainfall contribution by the
676 height spectrum of precipitation systems and associated cloud bulk properties over the South Asia, International Journal of
677 Climatology, 40, 3771–3791, https://doi.org/10.1002/joc.6427, 2020.
678 Ryu, J., Song, H.-J., Sohn, B.-J., and Liu, C.: Global distribution of three types of drop size distribution representing heavy
679 rainfall from GPM/DPR measurements, Geophysical Research Letters, 48, e2020GL090871,
680 https://doi.org/10.1029/2020GL090871, 2021.
681 Saha, P., Majumder, S., and Maitra, A.: Rain drop size distribution analysis at a tropical location near land-sea boundary,
682 Theor Appl Climatol, 147, 487–498, https://doi.org/10.1007/s00704-021-03809-4, 2022.
683 Seela, B. K., Janapati, J., Lin, P.-L., Wang, P. K., and Lee, M.-T.: Raindrop size distribution characteristics of summer and
684 winter season rainfall over North Taiwan, Journal of Geophysical Research: Atmospheres, 123, 11,602-11,624,
685 https://doi.org/10.1029/2018JD028307, 2018.

Shi, R., Lu, C., Xu, W., and Luo, Y.: A global view on microphysical discriminations between heavier and lighter convective rainfall, Commun Earth Environ, 6, 511, https://doi.org/10.1038/s43247-025-02473-0, 2025.

Skofronick-Jackson, G., Petersen, W. A., Berg, W., Kidd, C., Stocker, E. F., Kirschbaum, D. B., Kakar, R., Braun, S. A., Huffman, G. J., Iguchi, T., Kirstetter, P. E., Kummerow, C., Meneghini, R., Oki, R., Olson, W. S., Takayabu, Y. N., Furukawa, K., and Wilheit, T.: The global precipitation measurement (GPM) mission for science and society, Bulletin of the American Meteorological Society, 98, 1679–1695, https://doi.org/10.1175/BAMS-D-15-00306.1, 2017.

Snook, N. and Xue, M.: Effects of microphysical drop size distribution on tornadogenesis in supercell thunderstorms, Geophysical Research Letters, 35, https://doi.org/10.1029/2008GL035866, 2008.

Sowan, B., Hong, T.-P., Al-Qerem, A., Alauthman, M., and Matar, N.: Ensembling validation indices to estimate the optimal number of clusters, Appl Intell, 53, 9933–9957, https://doi.org/10.1007/s10489-022-03939-w, 2023.

Suh, S.-H., You, C.-H., and Lee, D.-I.: Climatological characteristics of raindrop size distributions in Busan, Republic of Korea, Hydrology and Earth System Sciences, 20, 193–207, https://doi.org/10.5194/hess-20-193-2016, 2016.

Sun, Y., Dong, X., Cui, W., Zhou, Z., Fu, Z., Zhou, L., Deng, Y., and Cui, C.: Vertical Structures of Typical Meiyu Precipitation Events Retrieved From GPM-DPR, Journal of Geophysical Research: Atmospheres, 125, e2019JD031466, https://doi.org/10.1029/2019JD031466, 2020.

Tapiador, F. J., Turk, F. J., Petersen, W., Hou, A. Y., García-Ortega, E., Machado, L. A. T., Angelis, C. F., Salio, P., Kidd, C., Huffman, G. J., and de Castro, M.: Global precipitation measurement: Methods, datasets and applications, Atmospheric Research, 104–105, 70–97, https://doi.org/10.1016/j.atmosres.2011.10.021, 2012.

Thompson, E. J., Rutledge, S. A., Dolan, B., and Thurai, M.: Drop size distributions and radar observations of convective and stratiform rain over the equatorial Indian and west Pacific Oceans, Journal of the Atmospheric Sciences, 72, 4091–4125, https://doi.org/10.1175/JAS-D-14-0206.1, 2015.

Uma, K. N. and Rao, T. N.: Characteristics of vertical velocity cores in different convective systems observed over Gadanki, India, Monthly Weather Review, 137, 954–975, https://doi.org/10.1175/2008MWR2677.1, 2009.

Wang, T. and Tang, G.: Spatial Variability and Linkage Between Extreme Convections and Extreme Precipitation Revealed by 22-Year Space-Borne Precipitation Radar Data, Geophysical Research Letters, 47, e2020GL088437, https://doi.org/10.1029/2020GL088437, 2020.

Wen, J., Wang, G., Zhou, R., Li, R., Zhaxi, S., and Bai, M.: Seasonal Variation in Vertical Structure for Stratiform Rain at Mêdog Site in Southeastern Tibetan Plateau, Remote Sensing, 16, 1230, https://doi.org/10.3390/rs16071230, 2024.

Wen, L., Chen, G., Yang, C., Zhang, H., and Fu, Z.: Seasonal variations in precipitation microphysics over East China based on GPM DPR observations, Atmospheric Research, 293, 106933, https://doi.org/10.1016/j.atmosres.2023.106933, 2023.

Wu, Z., Zhang, Y., Zhang, L., Zheng, H., and Huang, X.: A comparison of convective and stratiform precipitation microphysics of the record-breaking typhoon In-Fa (2021), Remote Sensing, 14, 344, https://doi.org/10.3390/rs14020344, 2022.

Zhang, Y. and Wang, K.: Global precipitation system size, Environ. Res. Lett., 16, 054005, https://doi.org/10.1088/1748-9326/abf394, 2021.

Zhang, Z., Li, H., Li, D., and Qi, Y.: Spatial variability of raindrop size distribution at Beijing city scale and its implications for polarimetric radar QPE, Remote Sensing, 15, 3964, https://doi.org/10.3390/rs15163964, 2023.

Zipser, E. J., Cecil, D. J., Liu, C., Nesbitt, S. W., and Yorty, D. P.: WHERE ARE THE MOST INTENSE THUNDERSTORMS ON EARTH?, Bull. Amer. Meteor. Soc., 87, 1057–1072, https://doi.org/10.1175/BAMS-87-8-1057, 2006.